PROCEEDINGS OF SPIE

SPIEDigitalLibrary.org/conference-proceedings-of-spie

Reflective lyot stop low-order wavefront control for future large space telescope coronagraphs

Christopher Mendillo, Jaren Ashcraft, Kevin Zhang Derby, Ewan Douglas, Daewook Kim, et al.

Christopher B. Mendillo, Jaren N. Ashcraft, Kevin Zhang Derby, Ewan S. Douglas, Daewook Kim, Jared Males, "Reflective lyot stop low-order wavefront control for future large space telescope coronagraphs," Proc. SPIE 12680, Techniques and Instrumentation for Detection of Exoplanets XI, 126802E (5 October 2023); doi: 10.1117/12.2677654

Event: SPIE Optical Engineering + Applications, 2023, San Diego, California, United States

Reflective Lyot stop low-order wavefront control for future large space telescope coronagraphs

Christopher B. Mendillo[a], Jaren N. Ashcraft[b], Kevin Zhang Derby[b], Ewan S. Douglas[b], Daewook Kim[b,c], and Jared Males[b]

[a]Lowell Center for Space Science and Technology, University of Massachusetts Lowell, 600 Suffolk Street Suite 315, Lowell, MA 01854, USA

[b]Department of Astronomy, University of Arizona, 933 N. Cherry Ave., Tucson, AZ 85721, USA

[c]James C. Wyant College of Optical Sciences, University of Arizona, 1630 E. University Blvd., Tucson, AZ 85721, USA

ABSTRACT

Future large space telescope missions for directly imaging exoplanets with internal coronagraphs will require picometer level low-order wavefront control to reach the 1×10^{-10} starlight suppression required to detect terrestrial exoplanets. This paper aims to characterize the reflective Lyot stop Low-Order Wavefront Sensor (LLOWFS) for the application where a transmissive focal plane mask is used, such as the Vector Vortex Coronagraph (VVC). This paper first defines the control requirements for such a mission based on the low-order tolerance of the VVC. The LLOWFS performance is then derived through optical simulation and compared to the requirements. The performance is calculated as a function of the target star brightness and aperture size and the final closed-loop stability is simulated using varying models for telescope pointing jitter and wavefront drift.

Keywords: exoplanets, wavefront control, direct imaging, fine pointing, high-contrast imaging

1. INTRODUCTION

Future large space telescope missions for directly imaging exoplanets with internal coronagraphs will require picometer level low-order wavefront control to reach the 1×10^{-10} starlight suppression required to detect terrestrial exoplanets.[1] The Astro2020 decadal survey[2] recommends at the highest priority a "Great Observatories Mission and Technology Maturation Program" that will work towards developing the future Habitable Worlds Observatory (HWO) flagship direct-imaging mission to characterize the atmospheres of potential life-hosting exoplanets. Recent studies for two such missions, Habitable Exoplanet Imaging Mission (HabEx)[3] and Large UV/Optical/IR Surveyor (LUVOIR),[4] have identified the vector vortex coronagraph (VVC) as a candidate coronagraph mask due to its efficiency, small inner working angle and tolerance to low-order aberrations. The VVC is transparent phase mask, an azimuthally rotating half-wave plate,[5] that diffracts all of the rejected on-axis starlight out of the pupil, where it is blocked by the Lyot stop. The reflective Lyot stop low-order wavefront sensor (LLOWFS) uses this bright signal that would otherwise be wasted to measure the wavefront error at the VVC location. This paper will investigate the suitability of the LLOWFS for use on future large space telescope missions to directly image exoplanets.

2. LOW-ORDER SENSITIVITY AND REQUIREMENTS

The VVC sensitivity to low-order aberrations is shown in Figure 1 for vortices of varying topological charge.[6] The aberrations are parameterized by the Zernike polynomials with coefficients expressed in units of root mean square (RMS) wavefront error. The sensitivity is calculated using an optical simulation built upon the Interactive Data Language (IDL) PROPER[7] library and the VVC model developed under the NASA Strategic Astrophysics

Further author information: (Send correspondence to C.B.M.)
C.B.M.: E-mail: christopher_mendillo@uml.edu

Techniques and Instrumentation for Detection of Exoplanets XI, edited by Garreth J. Ruane, Proc. of SPIE Vol. 12680, 126802E · © 2023 SPIE
0277-786X · doi: 10.1117/12.2677654

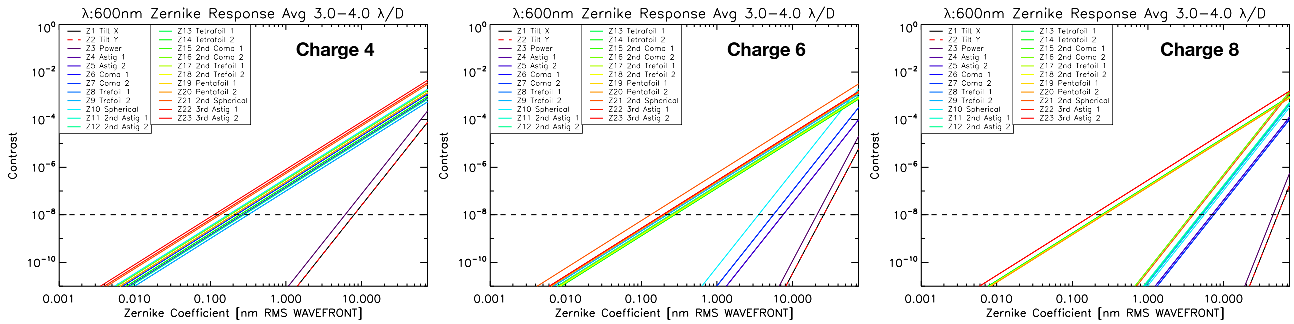

Figure 1. VVC leakage response to low-order wavefront error for the first 23 Zernike terms. The power-law response is plotted for charge 4, 6 and 8 vortices and the leakage is quantified as the contrast averaged over the annular region from 3-4 λ/D. A dashed line at 1×10^{-8} is shown for reference.

Technology (SAT)[8,9] program. Similar sensitivity curves can be found in previous works[1,6,10] discussing the low-order tolerance of the VVC. The VVC sensitivity has a clear power-law relationship described by Eq. 1.

$$Log[C] = ALog[Z] + B \quad \Longrightarrow \quad C = 10^B Z^A \tag{1}$$

We wish to convert these individual leakage curves into Zernike requirements for a given target contrast ratio. If we assume the residual Zernike errors, after low-order wavefront control (LOWFC), follow a Gaussian distribution, we can write down the time-averaged contrast value $\langle C \rangle$ as the gaussian-weighted integral of Eq. 1.

$$\langle C \rangle = 2\int_0^\infty 10^B Z^A \frac{1}{\sigma\sqrt{2\pi}} e^{\frac{-Z^2}{2\sigma^2}}\, dZ = \frac{2^{A/2}10^B\sigma^A}{\sqrt{\pi}}\Gamma\left(\frac{A+1}{2}\right) \tag{2}$$

Solving Eq. 1 for σ_Z, we have an expression for the required Zernike error to reach a given contrast. Note, σ_Z is the standard deviation (in time) of the Zernike coefficient.

$$\sigma_Z \approx 0.5\frac{1}{\sqrt{2}}\left(\frac{\sqrt{\pi}\langle C \rangle}{B\Gamma\left(\frac{A+1}{2}\right)}\right)^{\frac{1}{A}} \tag{3}$$

Eq. 3 gives a simple relationship for the required LOWFC residual of a single Zernike term. To produce an ensemble requirement of many Zernike terms, the target contrast should be divided by the number of terms such that each term produces the same amount of leakage. Note, the additional factor of 0.5 is empirically derived through simulation. Further work is required to finalize this formal derivation and understand the reason for this extra factor. We note, the factor should only be applied to Zernikes with power-law indices $A > 2$. Future work will attempt a fully analytical derivation of Eq. 3 that does not rely on optical simulation.

The best-fit power-law terms (A,B) are given in Table 1 alongside the ensemble LOWFC residual requirements for the first 23 Zernike terms. As the VVC charge increases, the coronagraph becomes more tolerant to the lowest-order Zernike terms due to an increase in their power law index (A) and decrease of their Y-intercept value (B).

3. REFLECTIVE LYOT STOP LOW-ORDER WAVEFRONT SENSOR

The LLOWFS[10–12] is an ideal choice for transmissive coronagraph masks such as the VVC, where all of the rejected starlight goes to the Lyot stop. A reflective stop and lens are used to focus the on-axis starlight to a detector that is placed slightly out of focus in order to spread the intensity pattern over many pixels. The intensity pattern responds linearly and near-orthogonally to low-order aberrations over a small dynamic range. The LLOWFS intensity response to the first 23 Zernikes is shown in Figure 2. These intensity values are placed

	Charge 4					Charge 6					Charge 8				
Z	A	B	$1x10^{-8}$	$1x10^{-9}$	$1x10^{-10}$	A	B	$1x10^{-8}$	$1x10^{-9}$	$1x10^{-10}$	A	B	$1x10^{-8}$	$1x10^{-9}$	$1x10^{-10}$
1	4	-11.60	1.378	0.775	0.436	6	-16.47	4.872	3.319	2.261	8	-21.74	9.854	7.389	5.541
2	4	-11.60	1.378	0.775	0.436	6	-16.47	4.872	3.319	2.261	8	-21.75	9.882	7.411	5.557
3	4	-11.13	1.051	0.591	0.332	6	-15.94	3.975	2.708	1.845	8	-21.24	8.533	6.399	4.798
4	2	-6.85	0.055	0.018	0.006	4	-11.50	1.301	0.732	0.411	4	-11.38	1.214	0.683	0.384
5	2	-6.85	0.055	0.018	0.006	4	-11.50	1.301	0.732	0.411	4	-11.38	1.214	0.683	0.384
6	2	-6.68	0.046	0.014	0.005	4	-10.99	0.970	0.545	0.307	4	-11.49	1.293	0.727	0.409
7	2	-6.68	0.046	0.014	0.005	4	-10.99	0.970	0.545	0.307	4	-11.49	1.293	0.727	0.409
8	2	-7.00	0.066	0.021	0.007	2	-6.68	0.046	0.014	0.005	4	-10.86	0.900	0.506	0.285
9	2	-7.00	0.066	0.021	0.007	2	-6.68	0.046	0.014	0.005	4	-10.86	0.900	0.506	0.285
10	2	-6.47	0.036	0.011	0.004	4	-10.20	0.616	0.346	0.195	4	-10.98	0.964	0.542	0.305
11	2	-6.89	0.058	0.018	0.006	2	-6.77	0.051	0.016	0.005	4	-10.76	0.850	0.478	0.269
12	2	-6.89	0.058	0.018	0.006	2	-6.77	0.051	0.016	0.005	4	-10.79	0.864	0.486	0.273
13	2	-6.78	0.051	0.016	0.005	2	-6.89	0.058	0.018	0.006	2	-6.77	0.051	0.016	0.005
14	2	-6.78	0.051	0.016	0.005	2	-6.88	0.057	0.018	0.006	2	-6.77	0.051	0.016	0.005
15	2	-6.52	0.038	0.012	0.004	2	-6.81	0.053	0.017	0.005	4	-10.31	0.656	0.369	0.207
16	2	-6.52	0.038	0.012	0.004	2	-6.81	0.053	0.017	0.005	4	-10.31	0.656	0.369	0.207
17	2	-6.62	0.043	0.013	0.004	2	-6.84	0.055	0.017	0.005	2	-6.81	0.053	0.017	0.005
18	2	-6.62	0.043	0.013	0.004	2	-6.84	0.055	0.017	0.005	2	-6.81	0.053	0.017	0.005
19	2	-6.62	0.043	0.013	0.004	2	-6.62	0.043	0.013	0.004	2	-6.84	0.055	0.017	0.005
20	2	-6.62	0.043	0.013	0.004	2	-6.62	0.043	0.013	0.004	2	-6.84	0.055	0.017	0.005
21	2	-6.26	0.028	0.009	0.003	2	-6.24	0.027	0.009	0.003	4	-10.40	0.691	0.388	0.218
22	2	-6.19	0.026	0.008	0.003	2	-6.56	0.040	0.013	0.004	2	-6.54	0.039	0.012	0.004
23	2	-6.09	0.023	0.007	0.002	2	-6.56	0.040	0.013	0.004	2	-6.55	0.039	0.012	0.004

Table 1. The best-fit power-law A and B values (Eq. 1) for the Zernike leakage response shown in Figure 1 are given for each vortex charge alongside the gaussian-weighted RMS Zernike requirements calculated using Eq. 3 (units are nm RMS wavefront error). Given the leakage requirement shown at the top of each column, the derived requirements assume a desired equal contribution of C/(N=23) from each Zernike mode.

into a response matrix and inverted using singular value decomposition (SVD) to create a LOWFS matrix that can be multiplied by an image (after proper normalization) to estimate a set of Zernike coefficients. The calibrated LLOWFS response (input vs. output) to individual Zernike terms is also shown in Figure 2 as well as the cross-coupling between terms. The system has two optical parameters, lens focal length and image defocus, that should be used to optimize the linear response and cross-coupling. Reducing LLOWFS cross-coupling between Zernike modes is of primary importance to the development of this sensor and may be aided in the future by machine learning techniques.

As a simplification to reduce simulation processing time, the remainder of this work will assume a perfect response function of the LLOWFS and focus instead on the effect of telescope aperture on the signal-to-noise ratio (SNR) of LLOWFS measurements and, in turn, the closed-loop LOWFC performance. These time-domain simulations of high-speed (100-1000 Hz) LOWFC require 10^5 iterations. To properly account for LLOWFS response and cross-coupling, a physical wavefront would need to be propagated through the system for each iteration, which would take 10^5 seconds on a standard workstation computer. Optimizing these simulations to make this possible in a reasonable amount of time is the next step.

To estimate the SNR of LLOWFS measurements, a throughput model of the optical system is required. A realistic, but best-case model is shown in Figure 3. This model assumes an un-obscured aperture and the minimum number of optics for a standard VVC coronagraph. The optical design consists of three telescope mirrors (primary, secondary and tertiary), four off-axis parabola (OAP) mirrors for relaying the pupil and imaging to the VVC mask, two deformable mirrors for high-order wavefront control and one low-order wavefront controller (a fast steering mirror or low-order deformable mirror). The LLOWFS consists of the reflective Lyot stop, a bandpass filter, a lens and the detector. For this study, the Sony IMX571 CMOS detector was chosen. The topological charge of the VVC affects the geometric throughput of the LLOWFS due to the dispersion pattern of the vortexed beam and the finite outer diameter of the Lyot stop. This is illustrated in Figure 4. VVC masks with lower charge produce a more centrally-concentrated pattern and thus result in more light reflected by the Lyot stop.

Using the throughput model shown in Figure 3 and the sensor noise characteristics of the IMX571 detector, realistic synthetic LLOWFS images can be simulated using the optical model. These images along with

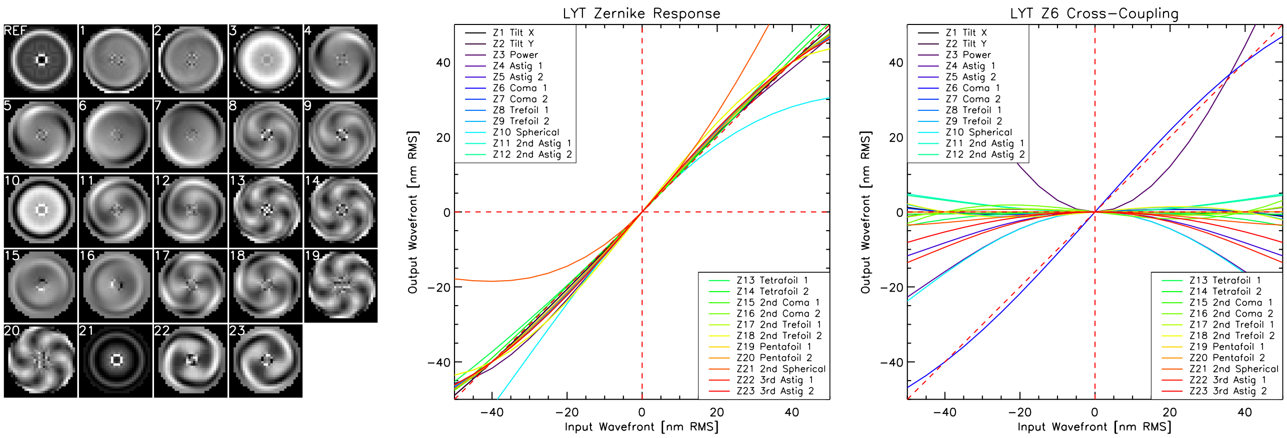

Figure 2. *Left:* LLOWFS detector images for each Zernike mode. Each image has the reference image (top left) subtracted out to show only the differential intensity pattern for that mode. *Middle:* LLOWFS response (input vs. output) to each mode. The response function is calibrated at ±40 nm, which is why most curves intersect the 1:1 line at those points. Calibration is most difficult for the first and second order spherical terms (Z10, Z21). *Right:* Cross-coupling between Z6 (Coma 1) and the other modes. In this design, there is strong coupling between Z6 and Z3.

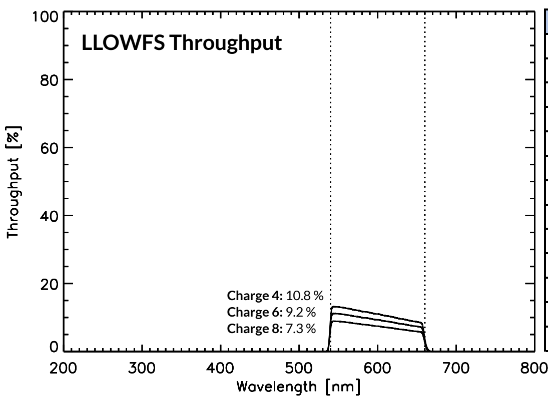

Surface	Comment	Quantity	Each		Combined
M1, M2	Protected Aluminum	2	89.9%	→	80.8%
M3, OAP1,2,3,4, Lyot Stop	Protected Silver	6	98.7%	→	92.4%
FSM or Low-Order DM	Protected Silver	1	97.9%	→	97.9%
VVC Transmission	VVC AR Coating	1	98.0%	→	98.0%
50% Polarization Loss	VVC Requires Pol. Filter	1	50.0%	→	50.0%
Linear Polarizer	LP Optical Transmission	1	71.4%	→	71.4%
Quarter Wave Plate	Clear glass + AR coating	1	97.5%	→	97.5%
BMC DM	Aluminum	2	89.8%	→	80.7%
Lyot Stop OD	Geometric loss (Charge 6)	1	74.3%	→	74.3%
Bandpass Filter	20% centered on 600 nm	1	89.9%	→	89.9%
Lens	Glass + AR coating	1	98.6%	→	98.6%
Detector	Sony IMX571	1	69.3%	→	69.3%
				Total:	9.2%

Figure 3. Throughput model for a 20% bandpass VVC coupled to a three-mirror telescope. The table to the right shows the efficiency of each optical surface and the figure to the left shows the bandpass throughput for three VVC charge values. The polarization filtering required by the VVC[5] creates the greatest reduction to system throughput with both the 50% loss of one polarization and the 71% transmission of the linear polarizer itself.

the LLOWFS response matrix are used to estimate the noise in Zernike measurements for differing telescope apertures, as shown in Figure 5.

4. CLOSED-LOOP LOWFC PERFORMANCE

The LLOWFS sensor noise model shown in Figure 5 can now be used to predict the close-loop performance of the LOWFC system in a given environment. The low-order disturbance environments presented here are a simple example based only on telescope pointing control. We assume a power-law spacecraft pointing power spectral density (PSD) with an index of -4 and varying RMS values of 10, 50 and 100 mas. An optical model of a compact 6.5 m space telescope[13] is used to calculate the Zernike errors at the VVC focal plane as a function of telescope pointing. No thermal or inertial disturbances to the optical alignment or surface deformations are included, only the off-axis wavefront error associated with the pointing offsets. This is the minimum error scenario. A full structure + thermal + optical + performance (STOP) model of the particular system would be required to produce a more realistic error signal. In this analysis, we assume the off-axis wavefront error scales with aperture size. Examples of the pointing and Zernike control are shown in Figure 6.

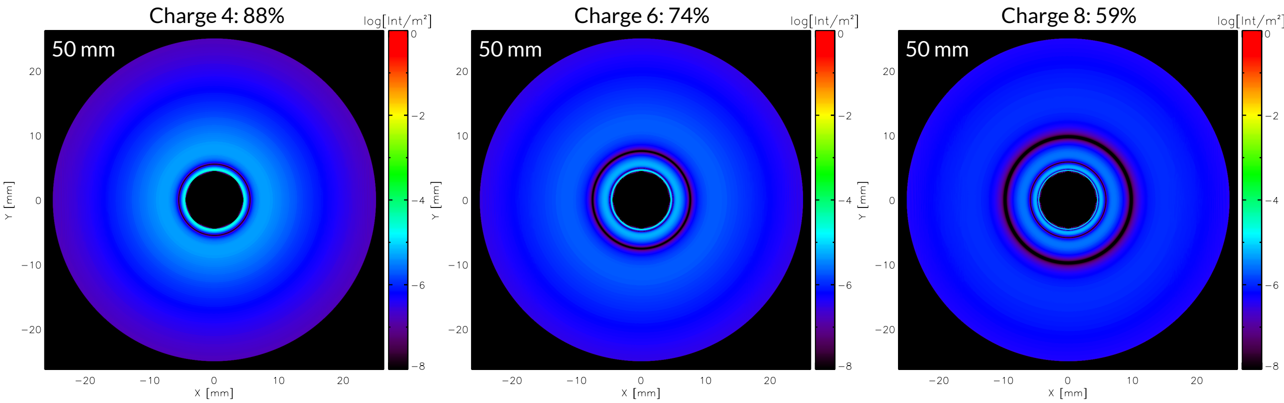

Figure 4. Post-VVC Lyot stop intensity patterns for charge 4, 6 and 8 vortices. Given a fixed outer Lyot stop diameter of 50 mm (5.6 times the nominal pupil diameter), the increased diffuseness of the intensity pattern with larger charges leads to a drop off in throughput due to vignetting. The geometric throughput is shown at the top of each map.

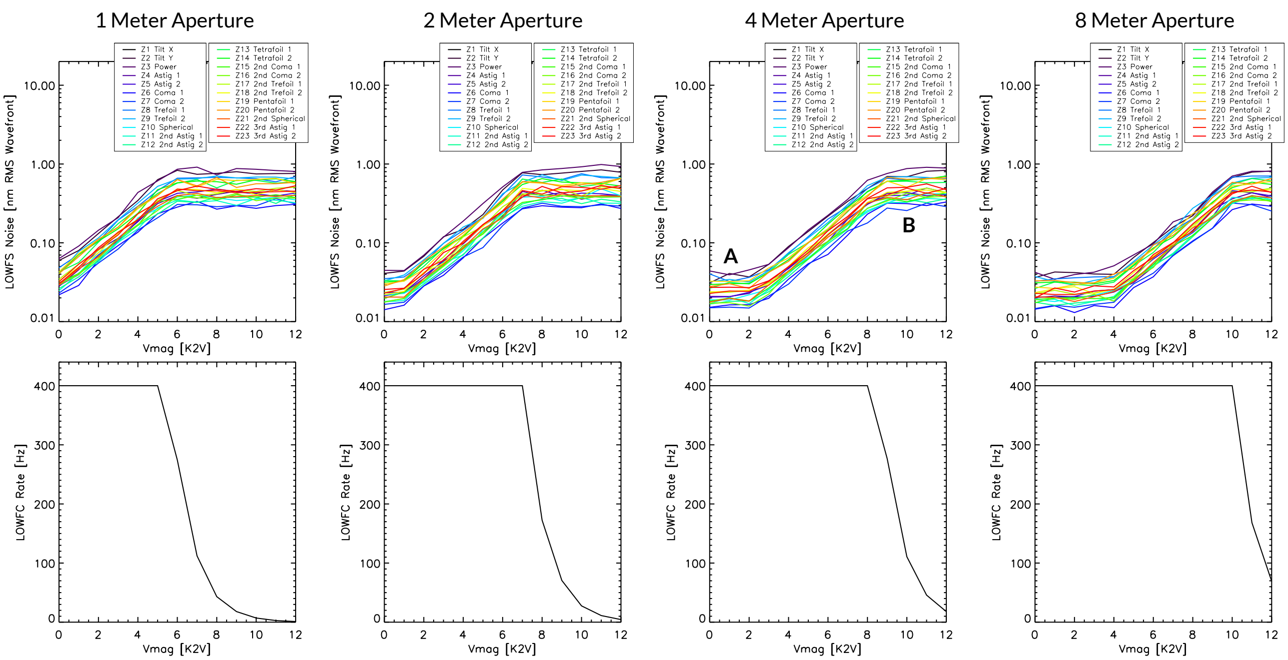

Figure 5. LLOWFS Zernike measurement noise as a function of stellar V-band magnitude for 1, 2, 4 and 8 meter telescope apertures (top row). The simulation uses a nominal exposure rate of 400 Hz and implements realistic exposure controls that affect the noise response. For bright signals (low Vmag), the exposure time is reduced to prevent saturation, but the frame rate is held at 400 Hz. For dim signals (high Vmag), the exposure time is increased and the frame rate is reduced accordingly to maintain a high enough signal level for accurate Zernike estimation (bottom row). These two measures cause the flattening seen at the bright and dim ends of the noise curves (marked A and B). The flattening at the bright end is simply the noise associated with an image at the full well capacity of the sensor. The frame rate could be increased at the bright end if required by the control system.

A

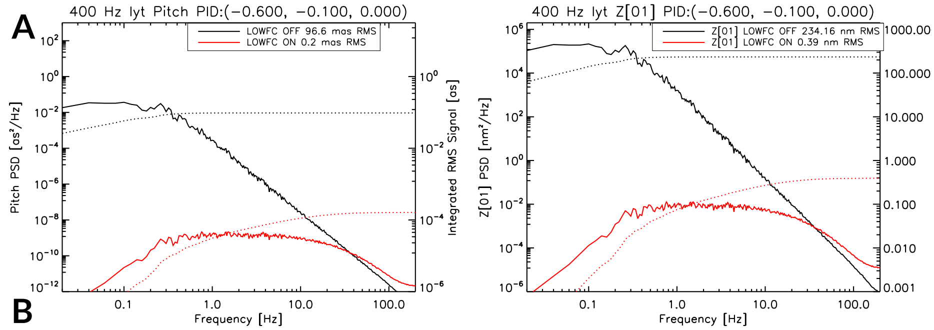

B

	Z	1	2	3	4	5	6	7	8	9	10	11	12
Pitch	nm/arcsec	-0.057	-0.019	-1.602	12.759	-1.036	-0.007	-0.020	-0.008	-0.058	-6.5E-05	1.4E-04	-5.2E-05
Yaw	nm/arcsec	0.013	-0.054	-3.006	-1.073	-12.677	-0.019	0.005	-0.057	0.008	-2.1E-04	1.1E-04	1.4E-04
	Z	13	14	15	16	17	18	19	20	21	22	23	
Pitch	nm/arcsec	1.3E-04	-3.5E-04	6.5E-06	-1.3E-05	6.5E-06	-2.0E-05	0	0	-6.5E-06	-6.5E-06	0	
Yaw	nm/arcsec	3.5E-04	1.3E-04	2.0E-05	6.5E-06	2.0E-05	6.5E-06	0	0	-6.5E-06	0	0	

C

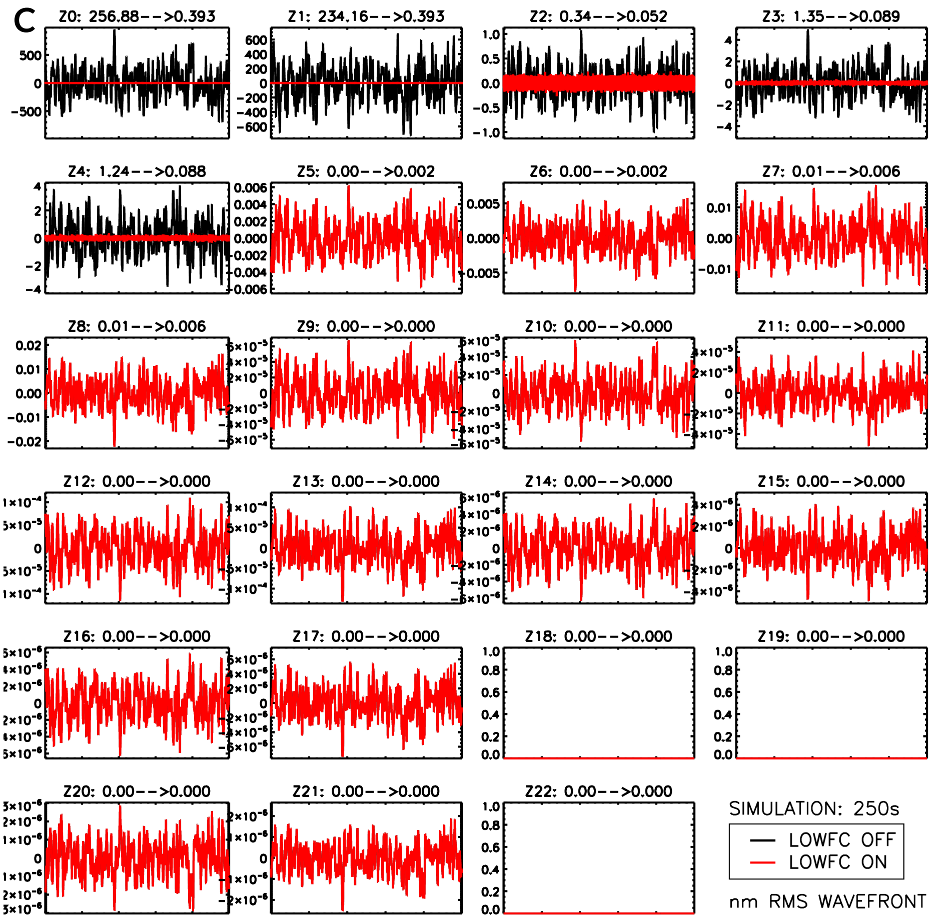

Figure 6. **A:** The telescope pointing error PSD is shown as the black line. This example shows a 100 mas RMS error with a -4 index power law. The error in telescope pitch is shown to the left and the corresponding Z1 (vertical tilt) error is shown to the right for the 2 meter aperture. **B:** Zernike error coefficients for the 2 meter aperture relating telescope pointing in arcseconds to RMS wavefront error in nanometers at the VVC focal plane. These values are multiplied by the pointing signal to produce the individual Zernike error signals. NOTE: the low-order errors used here are scaled linearly with telescope aperture. **C:** Time series of predicted Zernike errors. The ambient error signal is shown in black and the LOWFC stabilized signals are shown in red. In this example, LOWFC is not required on many of the modes due to low-amplitude errors. In those cases, control is disabled and the open/closed loop signals are the same. The top of each plot shows the reduction of the RMS error.

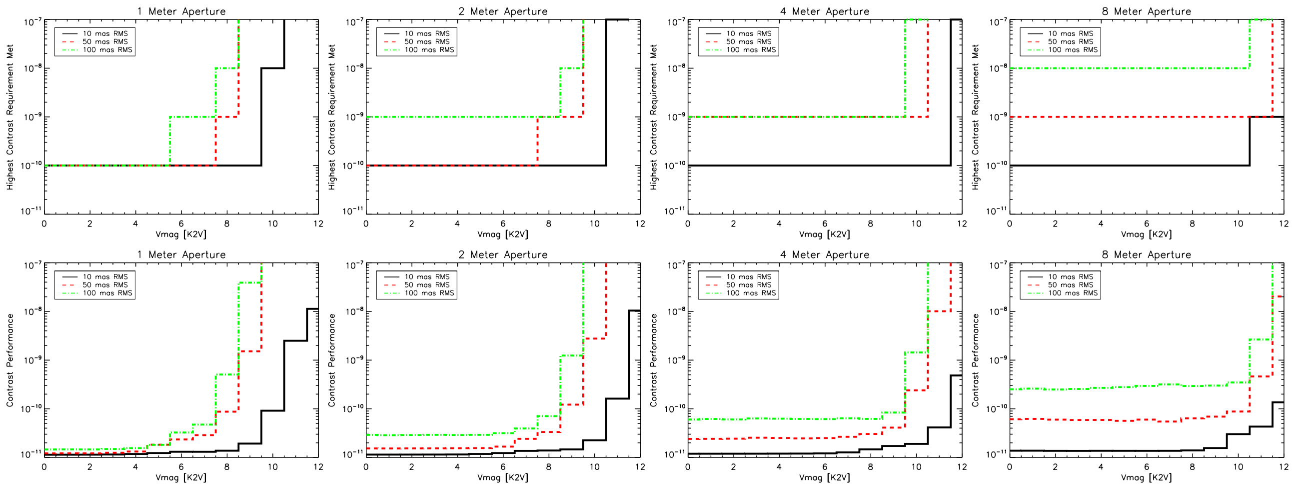

Figure 7. *Top Row:* Evaluation of contrast requirements for 10, 50 and 100 mas RMS telescope pointing driving low-order wavefront error and corrected in closed-loop with the LOWFC system. Plots are shown for each aperture size. In order for a simulation run to pass a contrast requirement, it must keep all 23 Zernikes below the requirements shown in Table 1. *Bottom Row:* Contrast performance values for each aperture size and pointing error. Here the result of each LOWFC simulation – a set of 23 Zernike residual sigma values – are passed off to the optical simulation and run with random Gaussian draws over 50 iterations to create a time-averaged contrast map. The average contrast over the 3-4 λ/D annulus is plotted as a function of V-band magnitude. The charge 6 VVC is used for all simulations. The increase in spread between the three pointing levels with increasing aperture size is due to the fact that the input low-order errors scale linearly with aperture size. Here the larger aperture is actually making the contrast performance worse because the extra light is not enough to improve the LOWFC performance proportionally. Further optimization of the LOWFC system may be able to improve this.

Finally, the closed loop LOWFC residuals can be compared with the requirements defined in Table 1. The plots in Figure 7 show the predicted contrast performance for each aperture in each pointing environment. Considering only the off-axis wavefront errors associated with telescope pointing, all aperture sizes were able to reach 1×10^{-10} contrast for stars with Vmag $<$ 10 and RMS pointing below 50 mas. The 8 meter aperture extended this range to Vmag = 12 with 10 mas pointing.

5. CONCLUSIONS

The LLOWFS is an ideal sensor to pair with the VVC due to its high efficiency and small image size, both of which enable high frame rates. The logarithmic response of the VVC to Zernike errors has allowed a simple, partially-analytical method for predicting the time-averaged contrast ratio in the presence of low-order wavefront error residuals and in turn defining low-order requirements for a given contrast ratio. Future work hopes to develop a fully analytical formulation of this method. While the VVC sensitivity curves are universally applicable, the LLOWFS and closed-loop LOWFC performance will depend on the optical system and low-order error operating environment. An example space telescope[13] with varying aperture size was used to illustrate the full analysis method required to predict the on-orbit coronagraph leakage due to low-order residuals. Considering only the off-axis wavefront errors associated with telescope pointing, all aperture sizes were able to reach 1×10^{-10} contrast for stars with Vmag $<$ 10 and RMS pointing below 50 mas. The 8 meter aperture extended this range to Vmag = 12 with 10 mas pointing. Flagship space telescopes such as the Hubble Space Telescope (HST) and the James Webb Space Telescope (JWST) have demonstrated spacecraft pointing well below 10 mas.[14,15] Figure 7 illustrates the importance of properly defining the LOWFC requirements. Defining an excessive number of Zernike requirements leads to the case where the requirement set is not fully met, even though the predicted performance is well below the top-level contrast requirement. These requirements should be defined only after the full low-order wavefront error environment is characterized. Individual Zernike requirements are useful when designing the low-order control system, but the top level contrast requirement should always be used to gauge the ultimate performance.

REFERENCES

[1] R. Juanola-Parramon, N. T. Zimmerman, L. Pueyo, M. Bolcar, Q. Gong, T. Groff, J. Krist, A. Roberge, G. Ruane, and C. Stark, "Modeling and performance analysis of the LUVOIR coronagraph instrument," **8**(03).

[2] N. A. of Sciences Engineering and Medicine, eds., *Pathways to Discovery in Astronomy and Astrophysics for the 2020s*, The National Academies Press, Washington, DC, 2021.

[3] https://www.jpl.nasa.gov/habex/. HabEx website.

[4] https://asd.gsfc.nasa.gov/luvoir/. LUVOIR website.

[5] D. Mawet, E. Serabyn, D. Moody, B. Kern, A. Niessner, A. Kuhnert, D. Shemo, R. Chipman, S. McClain, and J. Trauger, "Recent results of the second generation of vector vortex coronagraphs on the high-contrast imaging testbed at jpl," *Proc. SPIE* **8151**, p. 81511D, Sept. 2011.

[6] D. Mawet, L. Pueyo, D. Moody, J. Krist, and E. Serabyn, "The vector vortex coronagraph: sensitivity to central obscuration, low-order aberrations, chromaticism, and polarization," *Proc. SPIE* **7739**, p. 14, July 2010.

[7] J. E. Krist, "Proper: an optical propagation library for idl," *Proc. SPIE* **6675**, p. 0, Sept. 2007.

[8] https://exoplanets.nasa.gov/exep/technology/TDEM-awards/. NASA SAT website.

[9] J. E. Krist, D. C. Moody, D. Mawet, J. T. Trauger, R. Belikov, S. B. Shaklan, O. Guyon, and R. J. Vanderbei, "End-to-end simulations of different coronagraphic techniques," *Proc. SPIE* **7440**, p. 16, Aug. 2009.

[10] C. B. Mendillo, J. Brown, J. Martel, G. A. Howe, K. Hewasawam, S. C. Finn, T. A. Cook, S. Chakrabarti, E. S. Douglas, D. Mawet, O. Guyon, G. Singh, J. Lozi, K. L. Cahoy, and A. D. Marinan, "The low-order wavefront sensor for the picture-c mission," in *Techniques and Instrumentation for Detection of Exoplanets VII*, *Proc. SPIE* **9605**, p. 19, Sept. 2015.

[11] G. Singh, F. Martinache, P. Baudoz, O. Guyon, T. Matsuo, N. Jovanovic, and C. Clergeon, "Lyot-based low order wavefront sensor for phase-mask coronagraphs: Principle, simulations and laboratory experiments," *PASP* **126**, pp. 586–594, June 2014.

[12] C. B. Mendillo, K. Hewawasam, J. Martel, T. Potter, T. A. Cook, and S. Chakrabarti, "The picture-c exoplanetary imaging balloon mission: First flight results and second flight preparation," in *Techniques and Instrumentation for Detection of Exoplanets X*, S. B. Shaklan and G. J. Ruane, eds., SPIE, aug 2021.

[13] D. Kim, H. Choi, and E. S. Douglas, "Compact three mirror anastigmat space telescope design using 6.5m monolithic primary mirror,"

[14] www.stsci.edu/hst/HST_overview/documents/multidrizzle/ch42.html. The HST Multidrizzle Handbook.

[15] J. Rigby, M. Perrin, M. McElwain, R. Kimble, S. Friedman, M. Lallo, R. Doyon, L. Feinberg, P. Ferruit, A. Glasse, M. Rieke, G. Rieke, G. Wright, C. Willott, K. Colon, S. Milam, S. Neff, C. Stark, J. Valenti, J. Abell, F. Abney, Y. Abul-Huda, D. S. Acton, E. Adams, D. Adler, J. Aguilar, N. Ahmed, L. Albert, S. Alberts, D. Aldridge, M. Allen, M. Altenburg, J. A. Marquez, C. A. de Oliveira, G. Andersen, H. Anderson, S. Anderson, I. Argyriou, A. Armstrong, S. Arribas, E. Artigau, A. Arvai, C. Atkinson, G. Bacon, T. Bair, K. Banks, J. Barrientes, B. Barringer, P. Bartosik, W. Bast, P. Baudoz, T. Beatty, K. Bechtold, T. Beck, E. Bergeron, M. Bergkoetter, R. Bhatawdekar, S. Birkmann, R. Blazek, C. Blome, A. Boccaletti, T. Boeker, J. Boia, N. Bonaventura, N. Bond, K. Bosley, R. Boucarut, M. Bourque, J. Bouwman, G. Bower, C. Bowers, M. Boyer, L. Bradley, G. Brady, H. Braun, D. Breda, P. Bresnahan, S. Bright, C. Britt, A. Bromenschenkel, B. Brooks, K. Brooks, B. Brown, M. Brown, P. Brown, A. Bunker, M. Burger, H. Bushouse, S. Cale, A. Cameron, P. Cameron, A. Canipe, J. Caplinger, F. Caputo, M. Cara, L. Carey, S. Carniani, M. Carrasquilla, M. Carruthers, M. Case, R. Catherine, D. Chance, G. Chapman, S. Charlot, B. Charlow, P. Chayer, B. Chen, B. Cherinka, S. Chichester, Z. Chilton, T. Chonis, M. Clampin, C. Clark, K. Clark, D. Coe, B. Coleman, B. Comber, T. Comeau, D. Connolly, J. Cooper, R. Cooper, E. Coppock, M. Correnti, C. Cossou, A. Coulais, L. Coyle, M. Cracraft, M. Curti, S. Cuturic, K. Davis, M. Davis, B. Dean, A. DeLisa, W. deMeester, N. Dencheva, N. Dencheva, J. DePasquale, J. Deschenes, O. H. Detre, R. Diaz, D. Dicken, A. DiFelice, M. Dillman, W. Dixon, J. Doggett, T. Donaldson, R. Douglas, K. DuPrie, J. Dupuis, J. Durning, N. Easmin, W. Eck, C. Edeani, E. Egami, R. Ehrenwinkler, J. Eisenhamer, M. Eisenhower, M. Elie, J. Elliott, K. Elliott, T. Ellis, M. Engesser, N. Espinoza, O. Etienne, M. Etxaluze, P. Falini,

M. Feeney, M. Ferry, J. Filippazzo, B. Fincham, M. Fix, N. Flagey, M. Florian, J. Flynn, E. Fontanella, T. Ford, P. Forshay, O. Fox, D. Franz, H. Fu, A. Fullerton, S. Galkin, A. Galyer, M. G. Marin, J. Gardner, L. Gardner, D. Garland, B. Garrett, D. Gasman, A. Gaspar, D. Gaudreau, P. Gauthier, V. Geers, P. Geithner, M. Gennaro, G. Giardino, J. Girard, M. Giuliano, K. Glassmire, A. Glauser, S. Glazer, J. Godfrey, D. Golimowski, D. Gollnitz, F. Gong, S. Gonzaga, M. Gordon, K. Gordon, P. Goudfrooij, T. Greene, M. Greenhouse, S. Grimaldi, A. Groebner, T. Grundy, P. Guillard, I. Gutman, K. Q. Ha, P. Haderlein, A. Hagedorn, K. Hainline, C. Haley, M. Hami, F. Hamilton, H. Hammel, C. Hansen, T. Harkins, M. Harr, J. Hart, Q. Hart, G. Hartig, R. Hashimoto, S. Haskins, W. Hathaway, K. Havey, B. Hayden, K. Hecht, C. Heller-Boyer, C. Henriques, A. Henry, K. Hermann, S. Hernandez, B. Hesman, B. Hicks, B. Hilbert, D. Hines, M. Hoffman, S. Holfeltz, B. J. Holler, J. Hoppa, K. Hott, J. Howard, R. Howard, A. Hunter, D. Hunter, B. Hurst, B. Husemann, L. Hustak, L. I. Ignat, G. Illingworth, S. Irish, W. Jackson, A. Jahromi, P. Jakobsen, L. James, B. James, W. Januszewski, A. Jenkins, H. Jirdeh, P. Johnson, T. Johnson, V. Jones, R. Jones, D. Jones, O. Jones, I. Jordan, M. Jordan, S. Jurczyk, A. Jurling, C. Kaleida, P. Kalmanson, J. Kammerer, H. Kang, S.-H. Kao, D. Karakla, P. Kavanagh, D. Kelly, S. Kendrew, H. Kennedy, D. Kenny, R. Keski-kuha, C. Keyes, R. Kidwell, W. Kinzel, J. Kirk, M. Kirkpatrick, D. Kirshenblat, P. Klaassen, B. Knapp, J. S. Knight, P. Knollenberg, R. Koehler, A. Koekemoer, A. Kovacs, T. Kulp, N. Kumari, M. Kyprianou, S. La Massa, A. Labador, A. L. Ortega, P.-O. Lagage, C.-P. Lajoie, M. Lallo, M. Lam, T. Lamb, S. Lambros, R. Lampenfield, J. Langston, K. Larson, D. Law, J. Lawrence, D. Lee, J. Leisenring, K. Lepo, M. Leveille, N. Levenson, M. Levine, Z. Levy, D. Lewis, H. Lewis, M. Libralato, P. Lightsey, M. Link, L. Liu, A. Lo, A. Lockwood, R. Logue, C. Long, D. Long, C. Loomis, M. Lopez-Caniego, J. L. Alvarez, J. Love-Pruitt, A. Lucy, N. Luetzgendorf, P. Maghami, R. Maiolino, M. Major, S. Malla, E. Malumuth, E. Manjavacas, C. Mannfolk, A. Marrione, A. Marston, A. Martel, M. Maschmann, G. Masci, M. Masciarelli, M. Maszkiewicz, J. Mather, K. McKenzie, B. McLean, M. McMaster, K. Melbourne, M. Melendez, M. Menzel, K. Merz, M. Meyett, L. Meza, C. Miskey, K. Misselt, C. Moller, J. Morrison, E. Morse, H. Moseley, G. Mosier, M. Mountain, J. Mueckay, M. Mueller, S. Mullally, J. Murphy, K. Murray, C. Murray, D. Mustelier, J. Muzerolle, M. Mycroft, R. Myers, K. Myrick, S. Nanavati, E. Nance, O. Nayak, B. Naylor, E. Nelan, B. Nickson, A. Nielson, M. Nieto-Santisteban, N. Nikolov, A. Noriega-Crespo, B. O'Shaughnessy, B. O'Sullivan, W. Ochs, P. Ogle, B. Oleszczuk, J. Olmsted, S. Osborne, R. Ottens, B. Owens, C. Pacifici, A. Pagan, J. Page, S. Park, K. Parrish, P. Patapis, L. Paul, T. Pauly, C. Pavlovsky, A. Pedder, M. Peek, M. Pena-Guerrero, K. Pennanen, Y. Perez, M. Perna, B. Perriello, K. Phillips, M. Pietraszkiewicz, J.-P. Pinaud, N. Pirzkal, J. Pitman, A. Piwowar, V. Platais, D. Player, R. Plesha, J. Pollizi, E. Polster, K. Pontoppidan, B. Porterfield, C. Proffitt, L. Pueyo, C. Pulliam, B. Quirt, I. Q. Neira, R. R. Alarcon, L. Ramsay, G. Rapp, R. Rapp, B. Rauscher, S. Ravindranath, T. Rawle, M. Regan, T. A. Reichard, C. Reis, M. E. Ressler, A. Rest, P. Reynolds, T. Rhue, K. Richon, E. Rickman, M. Ridgaway, C. Ritchie, H.-W. Rix, M. Robberto, G. Robinson, M. Robinson, O. Robinson, F. Rock, D. Rodriguez, B. R. Del Pino, T. Roellig, S. Rohrbach, A. Roman, F. Romelfanger, P. Rose, A. Roteliuk, M. Roth, B. Rothwell, N. Rowlands, A. Roy, P. Royer, P. Royle, C. Rui, P. Rumler, J. Runnels, M. Russ, Z. Rustamkulov, G. Ryden, H. Ryer, M. Sabata, D. Sabatke, E. Sabbi, B. Samuelson, B. Sapp, B. Sappington, B. Sargent, A. Sauer, S. Scheithauer, E. Schlawin, J. Schlitz, T. Schmitz, A. Schneider, J. Schreiber, V. Schulze, R. Schwab, J. Scott, K. Sembach, C. Shanahan, B. Shaughnessy, R. Shaw, N. Shawger, C. Shay, E. Sheehan, S. Shen, A. Sherman, B. Shiao, H.-Y. Shih, I. Shivaei, M. Sienkiewicz, D. Sing, M. Sirianni, A. Sivaramakrishnan, J. Skipper, G. Sloan, C. Slocum, S. Slowinski, E. Smith, E. Smith, D. Smith, C. Smith, G. Snyder, W. Soh, T. Sohn, C. Soto, R. Spencer, S. Stallcup, J. Stansberry, C. Starr, E. Starr, A. Stewart, M. Stiavelli, A. Straughn, D. Strickland, J. Stys, F. Summers, F. Sun, B. Sunnquist, D. Swade, M. Swam, R. Swaters, R. Swoish, J. M. Taylor, R. Taylor, M. T. Plate, M. Tea, K. Teague, R. Telfer, T. Temim, D. Thatte, C. Thompson, L. Thompson, S. Thomson, T. Tikkanen, W. Tippet, C. Todd, S. Toolan, H. Tran, E. Trejo, J. Truong, C. Tsukamoto, S. Tustain, H. Tyra, L. Ubeda, K. Underwood, M. Uzzo, J. Van Campen, T. Vandal, B. Vandenbussche, B. Vila, K. Volk, G. Wahlgren, M. Waldman, C. Walker, M. Wander, C. Warfield, G. Warner, M. Wasiak, M. Watkins, A. Weaver, M. Weilert, N. Weiser, B. Weiss, S. Weissman, A. Welty, G. West, L. Wheate, E. Wheatley, T. Wheeler, R. White, K. Whiteaker, P. Whitehouse, J. Whiteleather, W. Whitman, C. Williams, C. Willmer, S. Willoughby, A. Wilson, G. Wirth, E. Wislowski, E. Wolf, D. Wolfe, S. Wolff, B. Workman, R. Wright, C. Wu, R. Wu, K. Wymer, K. Yates, C. Yeager, J. Yeates, E. Yerger,

J. Yoon, A. Young, S. Yu, D. Zak, P. Zeidler, J. Zhou, T. Zielinski, C. Zincke, and S. Zonak, "The science performance of jwst as characterized in commissioning," 2022.